Rare Metal Materials and Engineering
Volume 51, Issue 6, June 2022
Available online at www.rmme.ac.cn

Science Press

Cite this article as: Yao Jingjing, Zhang Di, Zhang Jishan. Study on Hot Deformation Behavior of Al-*x*Mg-2.8Zn Alloy by Constitutive Equations and Processing Maps[J]. Rare Metal Materials and Engineering, 2022, 51(06): 2046-2055.

ARTICLE

Study on Hot Deformation Behavior of Al-*x*Mg-2.8Zn Alloy by Constitutive Equations and Processing Maps

Yao Jingjing[1], Zhang Di[1,2], Zhang Jishan[1,2]

[1] State Key Laboratory of Advanced Metals and Materials, University of Science and Technology Beijing, Beijing 100083, China; [2] Beijing Laboratory of Metallic Materials and Processing for Modern Transportation, University of Science and Technology Beijing, Beijing 100083, China

Abstract: The hot deformation behavior of Al-*x*Mg-2.8Zn alloys at deformation temperature of 300~490 °C, strain rate of 0.001~5 s^{-1} was studied by isothermal hot compression tests. After correcting the flow softening from deformation heating in stress-strain curves, Arrhenius-type constitutive equations and processing maps were used to predict and analyze the hot deformation behavior of Al-*x*Mg-2.8Zn alloys. The results show that the flow stress increases with increasing Mg content and strain rate or decreasing temperature. According to the processing maps and corresponding microstructure of alloys, the range of optimum hot deformation parameters of alloys is determined. The range of hot deformation temperature and strain rate both extend and the instability domains extend to the zone of higher temperature and lower strain rate with increasing the Mg content.

Key words: Al-Mg-Zn alloy; hot deformation behavior; constitutive equation; processing map

Al-Mg-Zn alloy, as a new generation of aluminum alloy with good comprehensive performance, has been brought into focus in the past decade[1,2]. The new type Al-Mg-Zn alloy is a crossover aluminum alloy based on 5xxx series alloy (Al-Mg alloy) modified with main alloying elements used in 7xxx series alloys (Al-Zn-Mg alloy), capable of offering high strength through precipitation strengthening with T-$Mg_{32}(AlZn)_{49}$ phase[3]. Meanwhile, the potential difference between precipitates and Al matrix in Al-Mg-Zn alloy is smaller than that of the traditional age-hardening 7xxx series alloys, which leads to a lower corrosion tendency[4]. However, a major obstacle is that a series of problems like fractures and cracking are prone to happen during the hot deformation, which restricts the application of Al-Mg-Zn alloys, and the degree of deterioration varies with the composition of the alloy. It is necessary to study the hot deformation behavior of the promising Al-Mg-Zn alloy for successful manufacture.

A considerable amount of studies have been undertaken to explore the hot deformation behavior and deformation mechanisms of aluminum alloys using constitutive analysis and processing maps[5,6]. Constitutive equation is always applied to correlate different variables, such as flow stress, strain, deformation temperature, and strain rate, which is a promising approach to predict the flow behavior of metals and alloys, such as work hardening and dynamic softening. In addition, it can analyze the hot deformation behavior of alloys through exploring the effect of parameters on activation energy. The activation energy represents the free energy barrier for dislocation slipping on slip planes and indicates the hot deformation ability of materials. Liu et al[7] found that Arrhenius models can predict the flow behavior of Al-Mg-Si-Mn-Cr alloy with AARE values of only 3.38% and then revealed the thermal activation mechanism during hot deformation through establishing processing maps. Processing maps constructed under the principles of dynamic material modeling (DMM) can clearly represent an insight into the intrinsic deformation mechanism based on the calculation of power consumption during deformation, and determine the optimal processing windows of alloys[8]. Ke et al[9] constructed 3D processing maps of AA7020 aluminum alloy and obtained

Received date: June 02, 2021
Foundation item: Major State Research and Development Program of China (2016YFB0300801); National Natural Science Foundation of China (51971019, 51571013)
Corresponding author: Zhang Di, Ph. D., Professor, State Key Laboratory of Advanced Metals and Materials, University of Science and Technology Beijing, Beijing 100083, P. R. China, Tel: 0086-10-82375844, E-mail: zhangdi@skl.ustb.edu.cn

the optimum processing parameters within the temperature range of 743~793 K and strain rate range of 0.004~0.05 s^{-1}, through identifying recrystallization zones in processing maps. Luo et al[10] adopted a newly developed Fe-Cr-Ni-Al-Nb superalloy and conducted a series of hot compression tests, and concluded that the optimum process parameters were 1050 °C/0.1 s^{-1} via identifying different DRX mechanisms. Therefore, the hot workability of alloys can be reflected from constitutive equations and processing maps.

In this study, the hot workability of Al-Mg-Zn alloys was investigated. The flow softening resulting from deformation heating was corrected and the strain-compensated Arrhenius models were established and kinetic calculation was conducted to predict the flow behavior of Al-*x*Mg-2.8Zn alloys. The processing maps of Al-*x*Mg-2.8Zn alloys were constructed to determine the optimum processing parameters of hot deformation. In addition, the influence of Mg content on processing maps and relevant microstructures were discussed.

1 Experiment

Table 1 is the chemical composition (wt%) of the studied alloys. The Mg content of Alloy 1, Alloy 2 and Alloy 3 was about 2.8wt%, 5.4wt% and 8.4wt%, respectively. The as-cast samples were homogenized at 445 °C for 24 h, and then at 490 °C for 24 h. Subsequently the samples were machined into cylindrical specimens (Φ10 mm×15 mm). Isothermal hot compression tests were carried out at different deformation temperatures (300, 350, 400, 450, 490 °C) and different strain rates (0.001, 0.01, 0.1, 1, 5 s^{-1}) using Gleeble-1500 thermo-simulator. Before compression, the specimens were heated to the preset temperature at a heating rate of 2 °C/s, and maintained for 180 s (Fig.1). Graphite slices were placed between specimens and chunk to reduce frictions. All specimens were quenched in water immediately after compression. Then, the deformed specimens were sectioned along their compression axis.

Microstructures were observed using optical microscope (OM, Zeiss MC80DX) and electron backscattering diffraction (EBSD) with a Zeiss Ultra 55 scanning electron microscopy (SEM) instrument. Samples for OM were polished and then etched with Keller's solution. EBSD samples were mechanically polished and then electro-polished with 5vol% $HClO_4$ acids in alcohol at a voltage of 25 V at −35 °C.

2 Results and Discussion

2.1 Flow behavior

During deformation process, part of mechanical work converts into deformation heat, resulting in temperature rise of the alloy and causing inaccurate measurement results. Thus, it is necessary to correct the as-measured flow stress to accurately predict the flow behavior. In this study, the temperature rise (ΔT) is calculated by Eq.(1)[11],

$$\Delta T = \frac{0.95\eta_{\text{temp}}}{\rho C_{\text{p}}}\int_0^{\varepsilon}\sigma \mathrm{d}\varepsilon \tag{1}$$

The constant of 0.95 is the part of mechanical work converting into heat, and the other part is consumed for microstructure change; ρ is the material density and it equals to 2.72 g/cm^3 for Alloy 1, 2.68 g/cm^3 for Alloy 2 and 2.64 g/cm^3 for Alloy 3; C_{p} is the specific heat and calculated according to the Neumann-Kopp rule[12] as shown in Table 2; $\dot{\varepsilon}$ and σ represent the strain and as-measured stress, respectively; η is the adiabatic correction factor calculated by Eq.(2)[13],

$$\eta_{\text{temp}} = \begin{cases} 0 & \dot{\varepsilon} \leqslant 10^{-3}\,\text{s}^{-1} \\ 0.316\lg\dot{\varepsilon} + 0.95 & 10^{-3}\,\text{s}^{-1} \leqslant \dot{\varepsilon} \leqslant 1.0\,\text{s}^{-1} \\ 0.95 & \dot{\varepsilon} \geqslant 1.0\,\text{s}^{-1} \end{cases} \tag{2}$$

Temperature rise of all studied alloys is 0 when deformed at strain rate of 0.001 s^{-1}, since there is enough time for the heat generated from deformation to dissipate into environment[14].

Thus, the compensation of deformation heating can be calculated as a function:

$$\Delta\sigma_T = \frac{Q}{Rn\alpha}\left(\frac{1}{T_0} - \frac{1}{T_0 + \Delta T}\right) \tag{3}$$

where $\Delta\sigma_T$ is the value of flow softening resulting from deformation heating; R, n, α and Q are the gas constant, the stress exponent, the stress co-factor and the activation energy, respectively; T_0 and $T_0 + \Delta T$ are the preset temperature and actual deformation temperature, respectively.

Fig. 2 presents the as-measured and corrected stress-strain

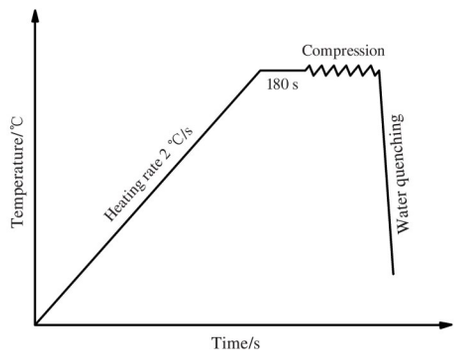

Fig.1 Schematic diagram of hot compression process

Table 1 Chemical composition of the studied Al-Mg-Zn alloys (wt%)

Alloy	Mg	Zn	Fe	Mn	Cu	Zr	Si	Ti	Cr	Al
1	2.8	2.8	0.15	0.25	0.05	0.15	0.15	0.07	0.03	Bal.
2	5.4	2.8	0.15	0.25	0.05	0.15	0.15	0.07	0.03	Bal.
3	8.4	2.8	0.15	0.25	0.05	0.15	0.15	0.07	0.03	Bal.

Table 2 Value of C_{p} of the studied alloys at different temperatures ($J\cdot g^{-1}\cdot k^{-1}$)

Alloy	C_{p}				
	300 °C	350 °C	400 °C	450 °C	490 °C
1	0.884	0.915	0.939	0.959	0.977
2	0.887	0.918	0.942	0.962	0.981
3	0.890	0.921	0.946	0.966	0.984

curves of three studied alloys during deformation under different deformation conditions. It is found that the flow stress curves display different trends under different deformation conditions. At the beginning of each deformation, a slight increase of strain causes a sharp increase of stress due to the effect of work hardening. With further increasing strain, these curves reflect the competition between work hardening and dynamic softening during hot deformation[5]. It is observed that the flow stresses of studied alloys are determined by processing parameters, which decrease with decreasing strain rate or increasing deformation temperature.

As deformation continues, various degrees of dynamic softening are seen in different alloys deformed at a given temperature and strain rate. The flow stress of Alloy 1 tends to increase after reaching the critical value, as shown in Fig. 2, while it gradually achieves a steady level when Mg content increases to 5.4wt% (Alloy 2), meaning that dynamic softening (DRX and DRV) and work hardening eventually reach a dynamic balance. As Mg content continues to increase (Alloy 3), the curves show a downward trend after it reaches a critical value. And Alloy 3 brakes when deformed at 490 °C, indicating that Mg content has a great influence on the flow behavior of Al-Mg-Zn alloys. The results indicate that the degree of dynamic softening increases with increasing Mg content. Moreover, it is also found that the peak stress increases with the increase of Mg content.

2.2 Constitutive equations

The relationship among flow stress (σ), strain rate ($\dot{\varepsilon}$) and deformation temperature (T) can be represented by Arrhenius model and Zener-Hollomon parameter (Z) as follows[15]:

$$Z = \dot{\varepsilon}\exp\left(\frac{Q}{RT}\right) = A_1\sigma^{n_1} \qquad \alpha\sigma < 0.8 \tag{4}$$

$$Z = \dot{\varepsilon}\exp\left(\frac{Q}{RT}\right) = A_2\exp(\beta\sigma) \qquad \alpha\sigma > 1.2 \tag{5}$$

$$Z = \dot{\varepsilon}\exp\left(\frac{Q}{RT}\right) = A\sinh(\alpha\sigma)^n \qquad \text{for all } \sigma \tag{6}$$

where R, Q are the ideal gas constant (8.314 J·mol^{-1}·K^{-1}) and the deformation activation energy (kJ·mol^{-1}), respectively; A, A_1, A_2, α, β, n and n_1 are constants of materials and $\alpha = \beta/n_1$. Taking natural logarithm on Eq.(4~6) :

$$\ln\dot{\varepsilon} = \ln A_1 + n_1\ln\sigma - \frac{Q}{RT} \tag{7}$$

$$\ln\dot{\varepsilon} = \ln A_2 + \beta\sigma - \frac{Q}{RT} \tag{8}$$

$$\ln\dot{\varepsilon} = \ln A + n\ln\left[\sinh(\alpha\sigma)\right] - \frac{Q}{RT} \tag{9}$$

According to Eq. (7~9), when the temperature is constant, the linear relationship of ln$\dot{\varepsilon}$-lnσ, ln$\dot{\varepsilon}$-σ and ln$\dot{\varepsilon}$-ln[sinh($\alpha\sigma$)] can be acquired through substituting the value of corrected data calculated above. The values of n_1 and β can be gained from the slopes of the plots of ln$\dot{\varepsilon}$-lnσ and ln$\dot{\varepsilon}$-σ, and α can also be obtained. The following equation can be gained from Eq.(9)

$$\ln\left[\sinh(\alpha\sigma)\right] = \frac{Q}{nRT} + \frac{1}{n}(\ln\dot{\varepsilon} - \ln A) \tag{10}$$

which means that ln[sinh($\alpha\sigma$)] and 1000/T are of linear relationship when strain rate is constant. And the value of Q can be calculated as

$$Q = R\left[\frac{\partial\ln\dot{\varepsilon}}{\partial\ln\left[\sinh(\alpha\sigma)\right]}\right]_T\left[\frac{\partial\ln\left[\sinh(\alpha\sigma)\right]}{\partial(1/T)}\right]_{\dot{\varepsilon}} \tag{11}$$

According to Eq. (11), the activation energy Q can be treated as a variable that is dependent on the deformation temperatures and strain rates. And the calculated Q value of studied alloys at peak stress is obtained using the peak stress adopted from the stress-strain curves, as shown in Fig. 3. It is seen that the activation energy decreases with increasing temperature in Alloy 1, while an opposite tendency is found in Alloy 2 and Alloy 3. The average Q value of Alloy 1, Alloy 2 and Alloy 3 is 170.3, 138.7 and 179.1 kJ·mol^{-1}. The activation energy (Q) is a significant indicator reflecting the hot deformation ability [16]. Previous studies have pointed that the region with constant and relatively high Q value in the activation energy map can be decided as a desirable processing zone[17]. Therefore, the possible processing window is marked with white rectangle in Fig. 3 and it is found that it tends to low temperature zone with increasing Mg content.

The value of Z can be determined based on Eq. (6) and taking natural logarithm of the equation gives

$$\ln Z = \ln A + n\ln\left[\sinh(\alpha\sigma)\right] \tag{12}$$

Thus, the values of ln$A$ and n can be determined. Based on Eq.(12), the flow stress can be determined as:

$$\sigma = \frac{1}{\alpha}\ln\left\{\left(\frac{Z}{A}\right)^{\frac{1}{n}} + \left[\left(\frac{Z}{A}\right)^{\frac{2}{n}} + 1\right]^{\frac{1}{2}}\right\} \tag{13}$$

Through repeating the above steps, the material constants (α, n, ln$A$ and Q) within the strain range between 0.05 and 0.7 with an interval of 0.05 can be gained. In addition, to obtain more accurate prediction, the equations should be revised by strain compensation. Generally, constructing polynomial functions of strain is an effective way to incorporate the effects of process parameters in constitutive equations[18]. In this study, a five-order polynomial function (Eq. (14)) is used to calculate these material constants (α, n, ln$A$ and Q) under various strains.

$$Y = V_0 + V_1\varepsilon + V_2\varepsilon^2 + V_3\varepsilon^3 + V_4\varepsilon^4 + V_5\varepsilon^5 \tag{14}$$

where Y represents the material constants (α, n, ln$A$ and Q), V_0 to V_5 are corresponding polynomial fitting coefficients listed in Table 3. The final strain compensated constitutive equations can be expressed as:

$$\begin{cases}\sigma(\varepsilon) = \dfrac{1}{\alpha(\varepsilon)}\ln\left\{\left(\dfrac{Z_{|Q(\varepsilon)|}}{A(\varepsilon)}\right)^{\frac{1}{n(\varepsilon)}} + \left[\left(\dfrac{Z_{|Q(\varepsilon)|}}{A(\varepsilon)}\right)^{\frac{2}{n(\varepsilon)}} + 1\right]^{\frac{1}{2}}\right\} \\ Z = \dot{\varepsilon}\exp\left(\dfrac{Q(\varepsilon)}{RT}\right)\end{cases} \tag{15}$$

The comparison between corrected and predicted stress is conducted in Fig. 4, purposing to verify the accuracy of the predicted results. The slope of the line fitted by these points is

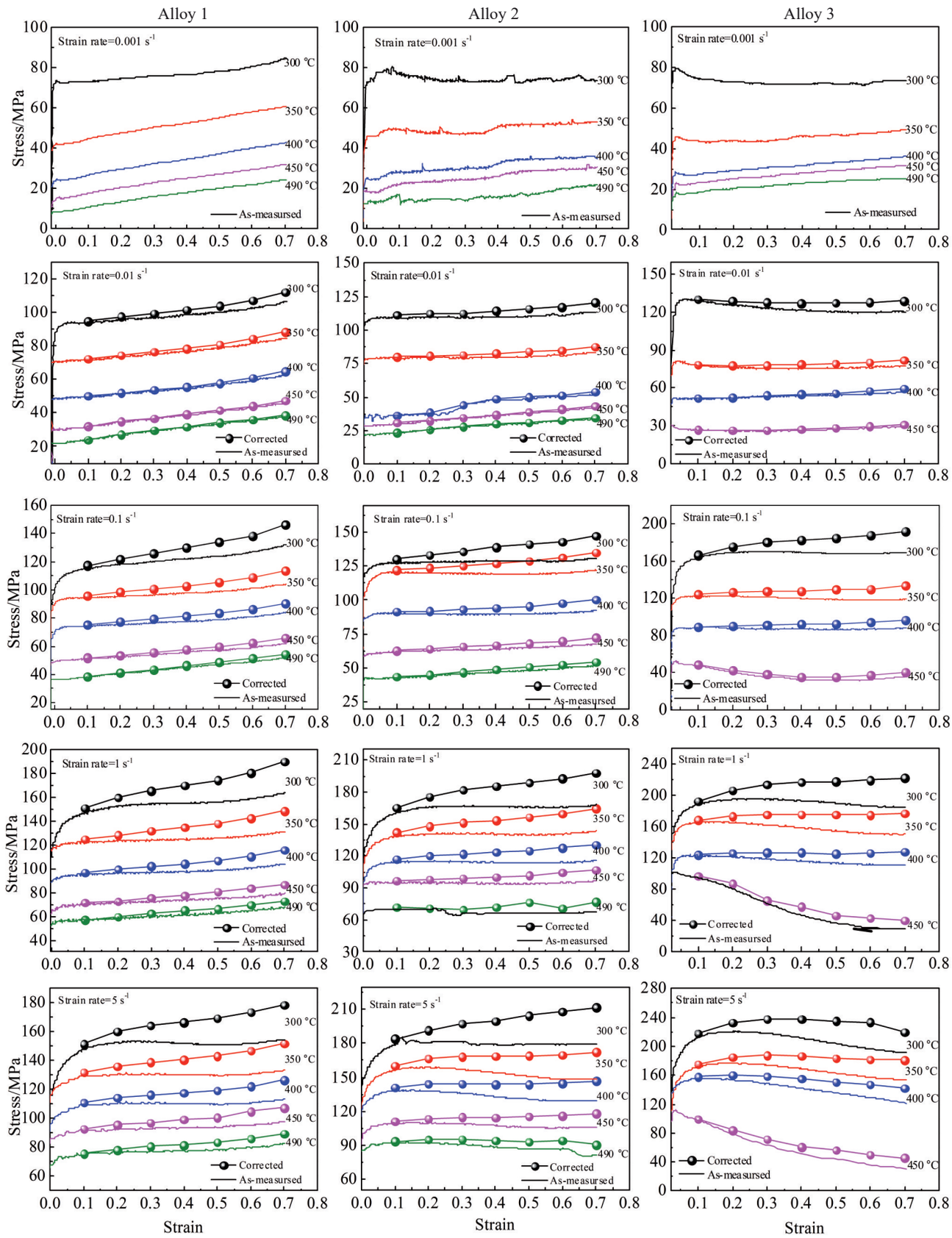

Fig.2 Stress-strain curves of alloys under different conditions

approximately 1 and the correlation coefficient (R^2) is 0.982, 0.975 and 0.984 for Alloy 1, Alloy 2 and Alloy 3, respectively. It means that predicted stress agrees well with corrected experimental stress and these constitutive equations predict

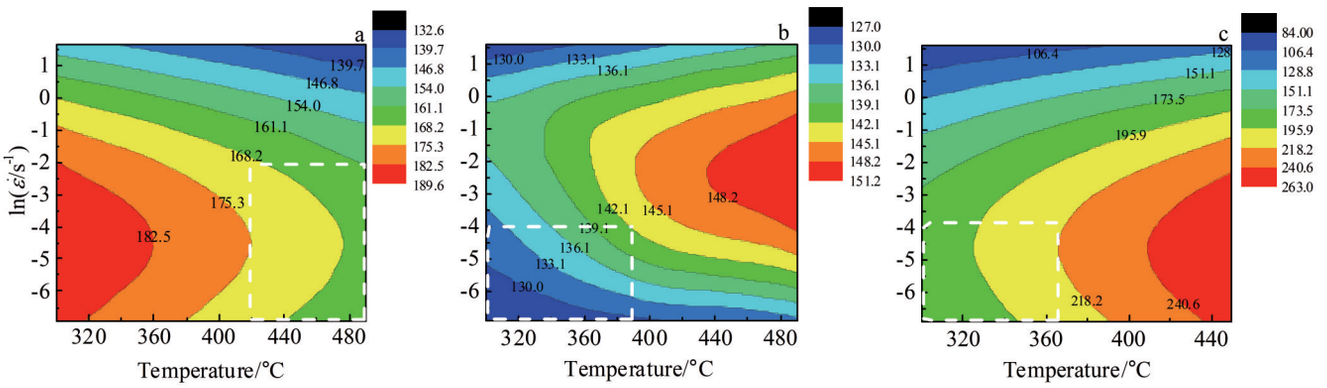

Fig.3 Activation energy Q of Alloy 1 (a), Alloy 2 (b) and Alloy 3 (c) during hot compression under different conditions

Table 3 Polynomial fitting coefficients V_0~V_5 of α, n, ln$A$ and Q for the studied alloys

Alloy	Constant	V_0	V_1	V_2	V_3	V_4	V_5
1	α/MPa^{-1}	0.018 9	0.075 79	0.645 29	2.278 91	3.724 05	2.225 27
	n	3.626 34	0.714 11	31.030 7	163.411	318.302	209.505
	ln$A$	19.101 7	13.061 5	181.815	687.337	1 109.65	626.552
	Q/kJ·mol^{-1}	19.101 6	13.061 6	181.816	687.337	1 109.65	626.552
2	α/MPa^{-1}	0.014 44	0.016 73	0.116 51	0.331 17	0.404 76	0.176 34
	n	4.148 9	2.780 12	25.971 4	102.628	144.592	66.639 3
	ln$A$	21.287 7	1.135 5	95.661 4	438.274	663.354	324.147
	Q/kJ·mol^{-1}	136 180.2	7 085.621	493 198.7	2 360 920	3 676 420	1 852 620
3	α/MPa^{-1}	0.017 29	0.016 99	0.047 1	0.066 56	0.034 46	0.003 17
	n	4.265 48	5.677 54	10.903 4	19.485	13.730 5	1.191 27
	ln$A$	23.553 6	8.781 22	16.390 6	45.653 8	181.196	141.713
	Q/kJ·mol^{-1}	150 171.7	52 541.87	111 466.9	137 900.8	799 927.4	667 834.5

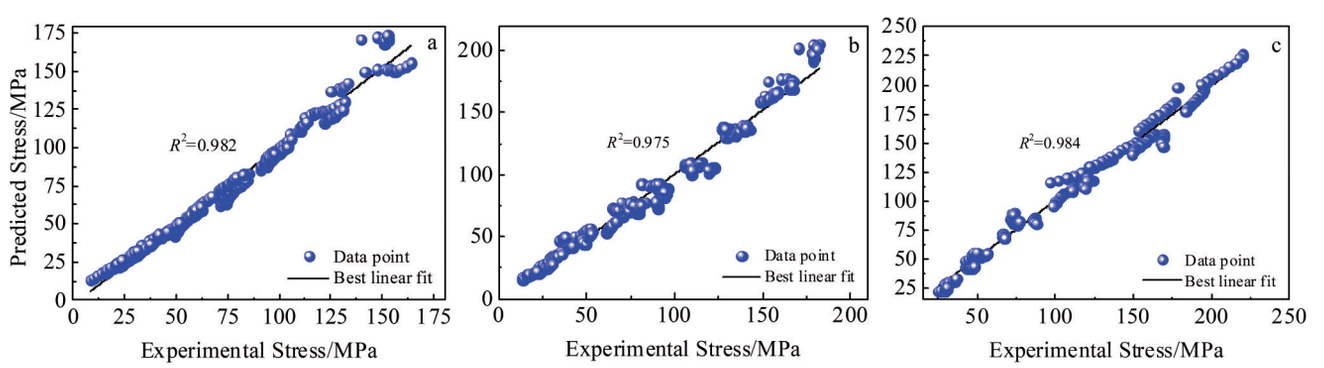

Fig.4 Comparison between corrected experimental stress and predicted stress of Alloy 1 (a), Alloy 2 (b) and Alloy 3 (c)

flow stress of studied alloys accurately.

2.3 Processing maps

Processing map can clearly show the stable and unstable zones of hot deformation parameters, which provides guidance for industrial production. According to the principles of the DMM[19], the deformation process involves power dissipation, and the total energy (P) is given as:

$$P = \sigma \cdot \dot{\varepsilon} = G + J = \int_0^{\dot{\varepsilon}} \sigma \mathrm{d}\dot{\varepsilon} + \int_0^{\sigma} \dot{\varepsilon} \mathrm{d}\sigma \tag{16}$$

where G is the energy loss caused by macroscopic plastic deformation, and J is the power dissipation caused by microstructural evolution, σ and $\dot{\varepsilon}$ represent the stress and strain rate, respectively, which are connected by introducing the strain rate sensitivity m assuming the power law nature of stress distribution [20],

$$\sigma = \dot{\varepsilon}^m \tag{17}$$

and thus, the total input power is partitioned between these two parts by strain rate sensitivity m:

$$m = \frac{\mathrm{d}J}{\mathrm{d}G} = \frac{\dot{\varepsilon}\mathrm{d}\sigma}{\sigma\mathrm{d}\dot{\varepsilon}} = \frac{\mathrm{d}\ln\sigma}{\mathrm{d}\ln\dot{\varepsilon}} \tag{18}$$

the derivative of cubic polynomial fitting the relationship between lnσ and ln$\dot{\varepsilon}$ is taken as the approximation value of m here, and J can be determined as:

$$J = \int_0^{\sigma} \dot{\varepsilon} \mathrm{d}\sigma = \frac{m}{m+1}\sigma\dot{\varepsilon} \tag{19}$$

During an ideal dissipation process, m=1 and J=J_{max}=($\sigma\dot{\varepsilon}$)/2. The power dissipation efficiency (η) can be represented as:

$$\eta = \frac{J}{J_{max}} = \frac{2m}{m+1} \tag{20}$$

Various values of power dissipation efficiency (η) obtained under different conditions are used to establish the 3D power dissipation map as shown in Fig.5. Different values of power dissipation efficiency are described with different colors. Generally, DRX is considered to be the main mechanism when the power dissipation efficiency is higher than 0.30[21], which can be classified as a safe zone in processing map. It is found that Mg contents and processing parameters have significant effects on power dissipation efficiency. The peak values of power dissipation efficiency are 0.38, 0.40, and 0.45 for Alloy 1, Alloy 2 and Alloy 3, respectively.

To explore whether flow instability occurs during hot deformation, the instability parameter $\xi(\dot{\varepsilon})$ is introduced to characterize the instability region, and it can be calculated as:

$$\xi(\dot{\varepsilon}) = \frac{\partial \lg\left[m/(m+1)\right]}{\partial \lg \dot{\varepsilon}} + m < 0 \tag{21}$$

Fig.6 shows the 3D instability maps of three studied alloys under different deformation conditions. Flow instability is prone to happen when $\xi(\dot{\varepsilon})$ is negative. The instability region ($\xi(\dot{\varepsilon})$<0) is shown by dark zone. It is found that the instability region increases with increasing strain. Moreover, some safe areas gradually transform into the instability region with increasing Mg content.

Processing maps of the three alloys are obtained by superimposing instability maps and power dissipation maps. Fig. 7 illustrates 2D processing maps of studied Al-Mg-Zn alloys under a true strain of 0.7. The dark area and the contour numbers represent the instability region and the value of power dissipation efficiency, respectively. And the optimum deformation parameter zones and instability region are marked as A and B, respectively. Zone A of Alloy 1 is located in the temperature range of 400~490 °C and strain rate range of 0.001~0.005 s^{-1}. As for Alloy 2, it is easier to deform in the temperature range of 300~390° C and strain rate range of 0.001~0.007 s^{-1}. When Mg content increases to 3wt%, zone A is in the temperature range of 300~420 ° C and strain rate range of 0.001~0.016 s^{-1}. It reflects that zone A extends to higher strain rate domain with increasing Mg content and the high Mg content extends the range of hot deformation temperature. In addition, it presents that the peak value of power dissipation efficiency increases from 0.38 to 0.40 and 0.45 with increasing Mg content. Moreover, the instability regions (zone B) expand to high temperature and low strain rate zones with increasing Mg content. In contrast, the instability domain of the new generation Al-Mg-Zn alloys is much smaller than that of traditional 7xxx alloys [22-24].

2.4 Microstructural observation

The optical microstructures of as-homogenized alloys are presented in Fig. 8a~8c. They are mainly composed of equiaxed grains and it is observed that the grain size decreases gradually with increasing Mg content, as shown in Fig.8d.

Fig. 9a~9f show the inverse pole figure (IPF) maps of the three studied alloys deformed under the same condition (400 °C/

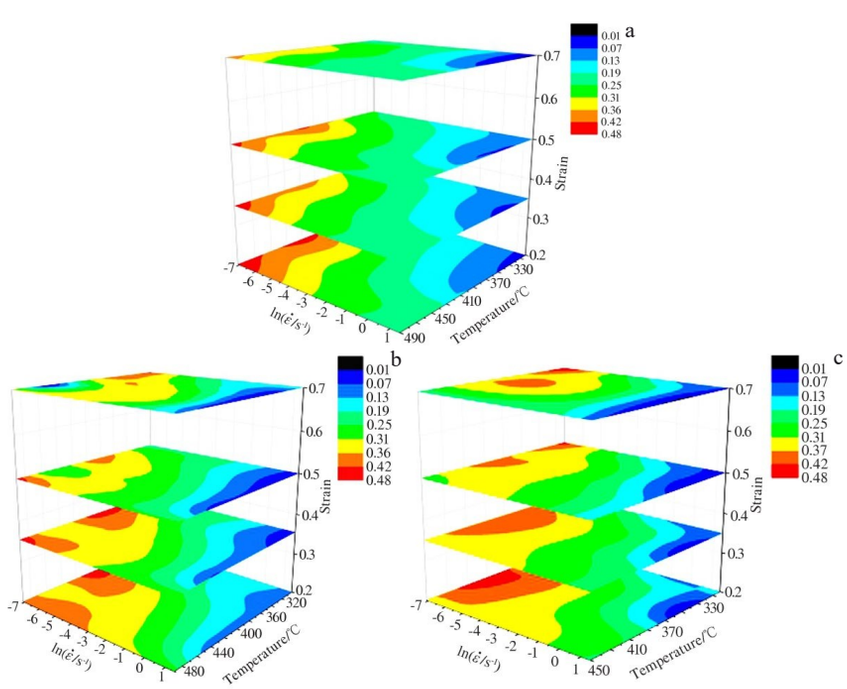

Fig.5 3D power dissipation maps of Alloy 1 (a), Alloy 2 (b) and Alloy 3 (c)

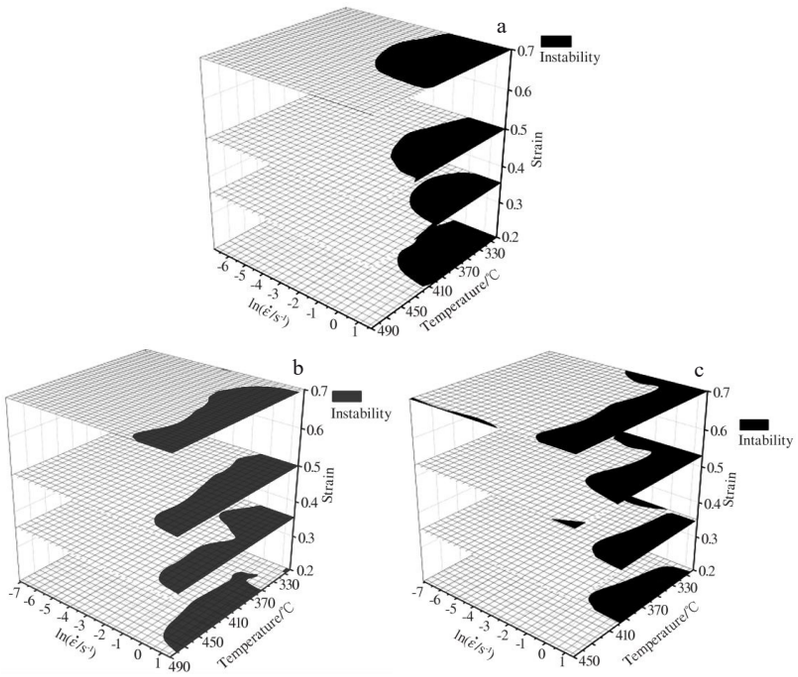

Fig.6 3D instability maps of Alloy 1 (a), Alloy 2 (b) and Alloy 3 (c)

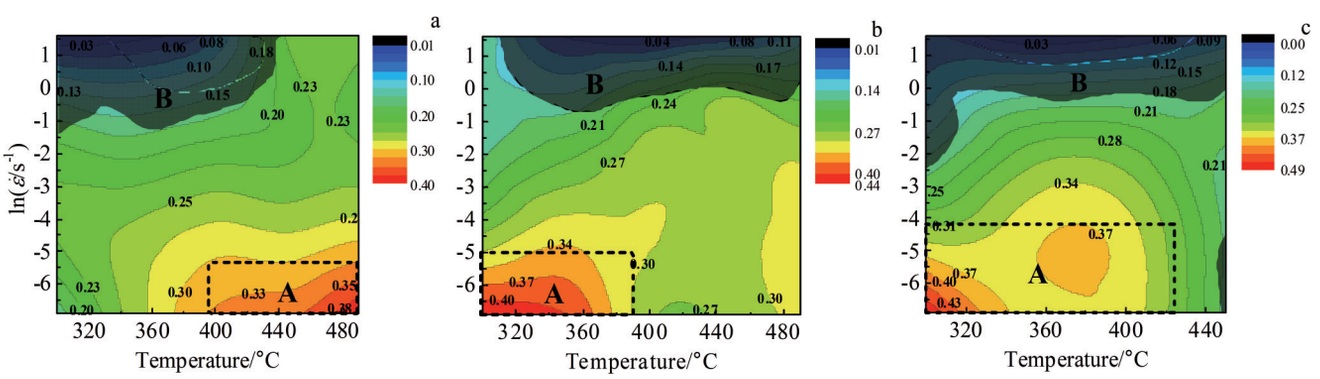

Fig.7 2D processing maps of Alloy 1 (a), Alloy 2 (b) and Alloy 3 (c) under a true strain of 0.7

0.001 s^{-1}), and the corresponding misorientation angle distribution maps are shown in Fig.9g~9i. Several finer grains adjacent to original grain observed in Alloy 1 and Alloy 3 mean that partial recrystallization occurs, while few are found in Alloy 2. According to the misorientation angle distribution maps presented in Fig. 9g~9i, the fraction of LAGBs firstly increases from 76% to 80% and then decreases to 65% with the increase of Mg content, reflecting that the extent of DRX grains first decreases and then increases with increasing Mg content in alloys. Fig. 9j~9l exhibit the corresponding kernel average misorientation (KAM) maps and various KAM value is represented with different color. Plastic deformation is accompanied by dislocation and grain boundary migration, and there will be serious misorientation and lattice distortion in these areas. The dislocation density (green line) with a high KAM value in the deformed grain is high and the distortion is serious, thereby, the dislocation movement can be activated while the thermal energy for overcoming energy barrier increases. It is seen that dislocation density is relatively low, which gives an explaination for the lower activation energy in Alloy2 compared with Alloy 1 and Alloy 3, as shown in Fig.3.

Dislocations are continuously generated and entangled during deformation process, and the stored energy accumulates rapidly and provides sufficient driving force for the movement of dislocations. Subsequently, the formation of subgrains results in separation of original grain boundaries, and accumulated energy is gradually consumed, indicating the occurrence of DRV. As deformation continues, subgrain boundary misorientation increases due to subgrain rotation, and eventually new grains form. This process is called CDRX, in which the fraction of LAGBs gradually decreases. It is well known that the main DRX mechanism of aluminum alloys with high stacking fault energy is CDRX, which occurs in Alloy 1. With decreasing the strain rate or increasing

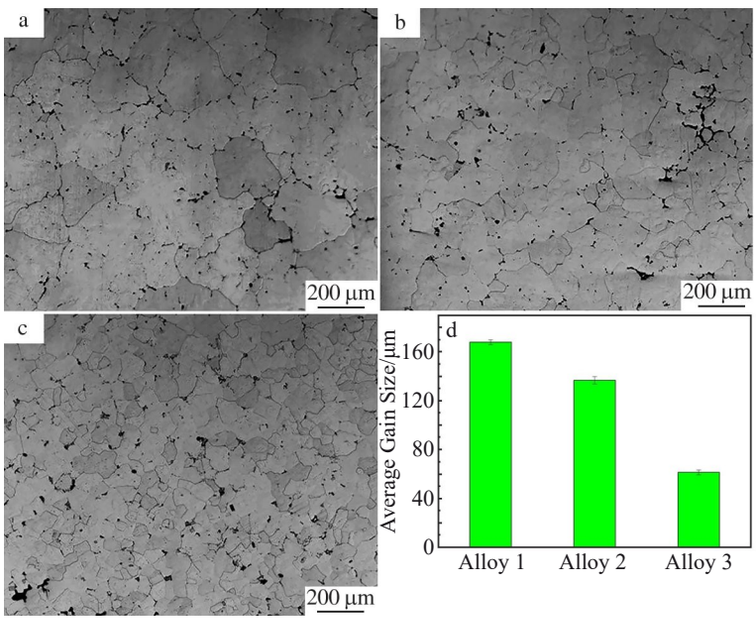

Fig.8 Optical microstructures of as-homogenized alloys (a~c) and average grain size of each alloy (d): (a) Alloy 1, (b) Alloy 2 and (c) Alloy 3

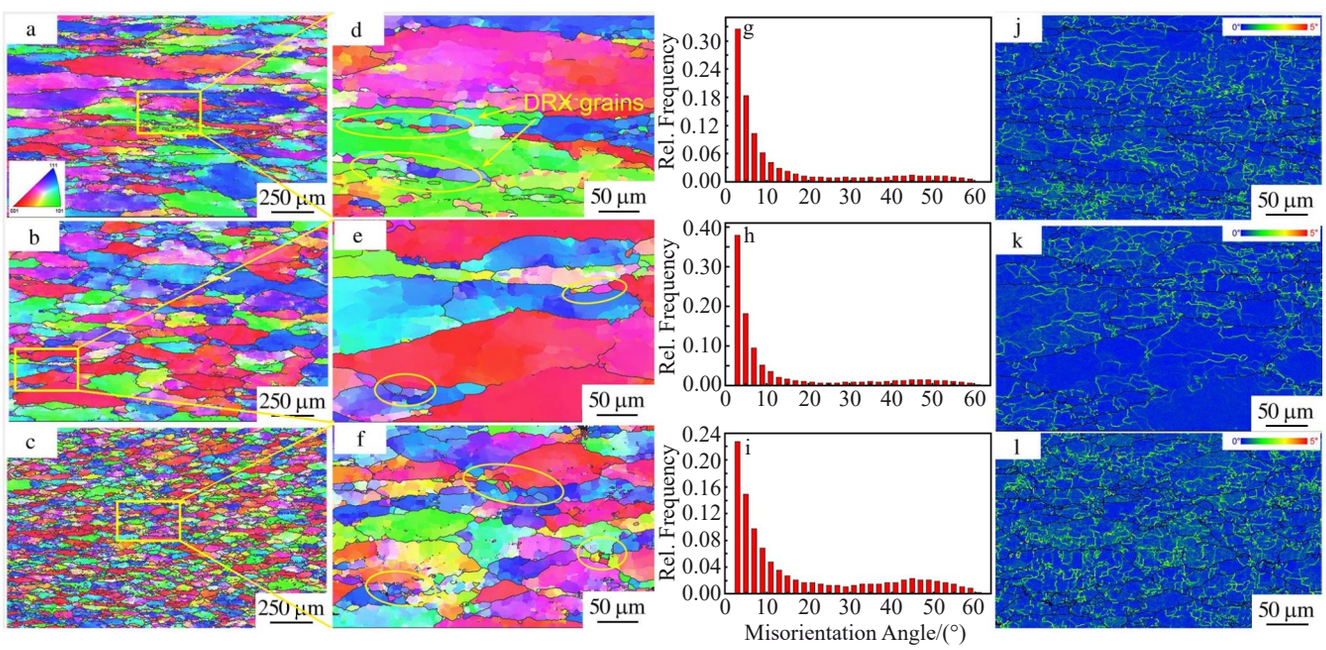

Fig.9 IPF maps (a, b, c) and corresponding enlarged images (d, e, f), misorientation angle distribution maps (g, h, i) and KAM maps (j, k, l) of Alloy 1 (a, d, g, j), Alloy 2 (b, e, h, k), Alloy 3 (c, f, i, l)

temperature, rearrangement and annihilation of the dislocation density occur due to increased extent of DRX in Alloy 1, leading to decrease of flow stress shown in Fig. 2, and the value of activation energy decreases (Fig. 3), so the alloy is suggested to process in the region of low strain rate and high temperature, which is consistent with process map of Alloy 1 (Fig.7a).

Differently, higher Mg content in Alloy 2 contributes to the decrease of stacking fault energy, and the DRV and CDRX are suppressed during hot deformation resulting from hindered movement of dislocations, which is the reason for the increase of flow stress and LAGBs transform into HAGBs. With continuously increasing the Mg content (Alloy 3), the accumulation of dislocation and energy is enough to provide a driving force for nucleation of new grains at HAGBs, and DDRX occurs, and thereby, the fraction of LAGBs decreases, reveling that DDRX occurs, which is the reason why flow soften is seen when Alloy 2 and Alloy 3 are deformed at high temperature, as shown in Fig. 2[25]. As a result, the optimum zone tends to low temperature zone with increasing Mg

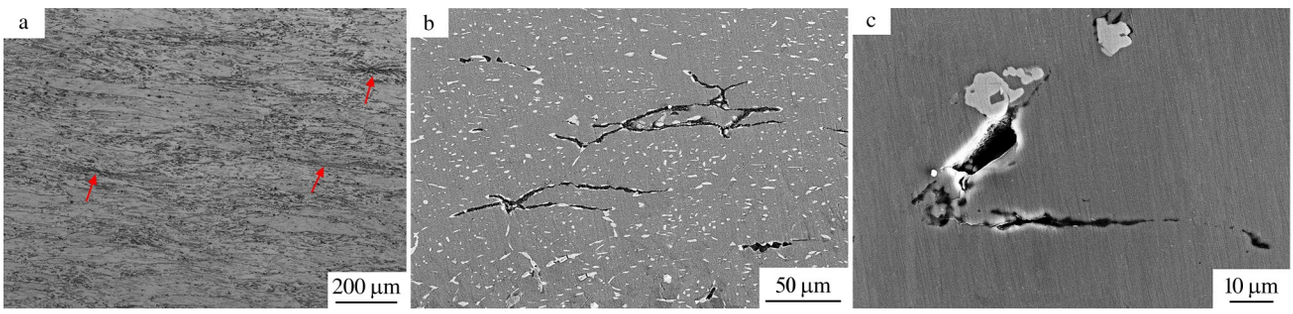

Fig.10 Micrographs of specimens deformed at instability region: (a) Alloy 1 at 400 °C/1 s^{-1}, (b) Alloy 2 at 350 °C/1 s^{-1}, and (c) Alloy 3 at 450 °C/5 s^{-1}

content, as presented in Fig.7.

The micrographs of the three studied alloys deformed at instability zones are displayed in Fig.10. Flow localization can be observed for Alloy 1 deformed at 400 °C/1 s^{-1}, as shown in Fig. 10a. At low temperature and high strain domains, flow localization is more prone to happen due to insufficient energy and time for uniform deformation. And it may be the source of defects such as microcracks for Alloy 2 deformed under 350 °C/1 s^{-1}, as shown in Fig. 10b, and it will develop into macroscopic cracks eventually. Fig.10c displays micro-cracks, particle breakage and voids resulting from stress accumulation near particles, which do not dissolve into the matrix when Alloy 3 is deformed at 450 °C/5 s^{-1}. These defects are undesirable for alloys and lowering the deformation temperature is an effective measurement to prepare sheet without defects for higher Mg content alloy, which is also verified in the kinetic calculations and processing maps.

3 Conclusions

1) The peak value of flow stress increases with increasing Mg content in Al-*x*Mg-2.8Zn alloy. The flow stress and the values of flow softening resulted from deformation heating both tend to increase with increasing strain rate or decreasing temperature. Constitutive analysis can predict the flow behavior of the three studied Al-Mg-Zn alloys with high accuracy.

2) Processing maps show that the range of hot deformation temperature and strain rate expands with increasing Mg content, and the instability domains extend to the zone of higher temperature and lower strain rate.

3) The value of power dissipation efficiency of the three studied alloys first increases and then decreases with increasing Mg content, which is due to the transformation from continuous to discontinuous dynamic recrystallization, and it proves the validity of processing maps.

References

1 Cao C, Zhang D, Zhuang L Z *et al. Journal of Alloys and Compounds*[J], 2017, 691: 40

2 Stemper L, Tunes M A, Oberhauser P *et al. Acta Materialia*[J], 2020, 195: 541

3 Pan Y L, Zhang D, Liu H R *et al. Journal of Alloys and Compounds*[J], 2020, 853: 157 199

4 Ding Q W, Zhang D, Zuo J R *et al. Materials Characterization* [J], 2018, 146: 47

5 Roy S, Suwas S. *Journal of Alloys and Compounds*[J], 2013, 548: 110

6 Zhong L W, Gao W L, Feng Z H *et al. Journal of Materials Science Technology*[J], 2019, 35(10): 2409

7 Liu S H, Pan Q L, Li H *et al. Journal of Materials Science*[J], 2019, 54(5): 4366

8 Che B, Lu L W, Kang W *et al. Journal of Alloys and Compounds* [J], 2021, 862(5): 158 700

9 Ke B, Ye L Y, Tang J G *et al. Journal of Alloys and Compounds* [J], 2020, 845: 156 113

10 Luo R, Chen L L, Zhang Y X *et al. Journal of Alloys and Compounds*[J], 2021, 865: 158 601

11 Goetz R L, Semiatin S L. *Journal of Materials Engineering and Performance*[J], 2001, 10(6): 710

12 Laan R R V D, Konings R J M. *Journal of Alloys and Compounds*[J], 2000, 297: 104

13 Shi Z X, Yan X F, Duan C H *et al. Transactions of Nonferrous Metals Society of China*[J], 2017, 27(3): 538

14 Qian L Y, Fang G, Zeng P *et al. International Journal of Pressure Vessels*[J], 2015, 132-133: 43

15 Ansari N, Tran B, Poole W J *et al. Materials Science and Engineering A*[J], 2020, 777: 139 051

16 Rezaee M, Zarei-Hanzaki A, Ghambari M *et al. Advanced Engineering Materials*[J], 2016, 18(6): 1075

17 Zhang J, Di H, Wang H *et al. Journal of Materials Science*[J], 2012, 47(9): 4000

18 Wu R H, Liu Y, Geng C *et al. Journal of Alloys and Compounds* [J], 2017, 731: 212

19 Prasad Y V R K, Gegel H L, Doraivelu S M *et al. Metallurgical Transactions A*[J], 1984, 15(10): 1883

20 Gang M, Li B, Li H *et al. Materials Science & Engineering A*[J], 2009, 517(1-2): 132

21 Li C M, Huang L, Zhao M J *et al. Materials Science and*

Engineering A[J], 2020, 797: 139 925

22 Lin Y C, Li L T, Xia Y C *et al. Journal of Alloys and Compounds* [J], 2013, 550: 438

23 Wang S, Hou L G, Luo J R *et al. Journal of Materials Processing Technology*[J], 2015, 225: 110

24 Park S Y, Kim W J. *Journal of Materials Science & Technology* [J], 2016, 32(7): 660

25 Sakai T, Belyakov A, Kaibyshev R *et al. Progress in Materials Science*[J], 2014, 60(1): 130

基于本构方程和热加工图的Al-*x*Mg-2.8Zn合金的热变形行为研究

姚晶晶[1]，张　迪[1,2]，张济山[1,2]

(1. 北京科技大学 新金属材料国家重点实验室，北京 100083)

(2. 北京科技大学 现代交通金属材料与加工技术北京实验室，北京 100083)

摘　要：通过热压缩模拟试验研究了Al-*x*Mg-2.8Zn合金在变形温度为300~490 ℃、应变速率为0.001~5 s^{-1}条件下的热变形行为。修正了应变-应力曲线中由于变形热引起的流动软化现象后，利用Arrhenius本构方程和热加工图预测并分析了Al-*x*Mg-8Zn合金的热变形行为。结果表明，随着Mg含量的增加，应变速率的升高，或者变形温度的降低，流变应力随之增大。结合热加工图和微观组织观察，确定了合金的最佳热加工参数范围。通过对比发现，随着Mg含量的增加，最佳热变形温度和应变速率范围均变大，变形失稳区域向高温和低应变速率区域扩展。

关键词：Al-Mg-Zn合金；热变形行为；本构方程；热加工图

作者简介：姚晶晶，女，1995年生，硕士，北京科技大学新金属材料国家重点实验室，北京 100083，E-mail：yaojj2376@163.com